Materials Science and Engineering B 185 (2014) 7–12

Contents lists available at ScienceDirect

Materials Science and Engineering B

journal homepage: www.elsevier.com/locate/mseb

Solvothermal synthesis of V_2O_5/graphene nanocomposites for high performance lithium ion batteries

Da Chen [1], Ran Yi, Shuru Chen, Terrence Xu, Mikhail L. Gordin, Dongping Lv, Donghai Wang*

Department of Mechanical & Nuclear Engineering, The Pennsylvania State University, University Park, PA 16802, USA

ARTICLE INFO

Article history:
Received 22 August 2013
Received in revised form 16 January 2014
Accepted 26 January 2014
Available online 9 February 2014

Keywords:
V_2O_5 nanoparticles
Graphene nanosheets
Solvothermal synthesis
Electrochemical performance
Lithium ion batteries

ABSTRACT

In this work, V_2O_5/graphene nanocomposites have been synthesized by a facile solvothermal approach. The V_2O_5 nanoparticles, around 20–40 nm in size, were encapsulated in the 2D graphene matrix. The reversible Li-cycling properties of V_2O_5/graphene have been evaluated by galvanostatic discharge–charge cycling, cyclic voltammetry, and impedance spectroscopy. Compared with the bare V_2O_5 nanoparticles, the V_2O_5/graphene nanocomposites exhibited enhanced electrochemical performance with higher reversible capacity and improved cycling stability and rate capability. The graphene nanosheets act not only as an electronically conductive matrix to improve the electronic and ionic conductivity of the composite electrode, but also as a flexible buffer matrix to maintain the structural integrity of the composite electrodes by preventing particle agglomeration, thus leading to the improvement of the electrochemical performance of V_2O_5.

1. Introduction

Lithium-ion batteries (LIBs), as a green and rechargeable power source, have attracted much more attention due to their extensive applications in portable electronic devices and electric vehicles [1]. Recent research trends in the field of LIBs are directed toward the development of cells with high specific energy and high energy density [2]. Many researchers have demonstrated that the energy storage capacity in a rechargeable lithium or lithium-ion cell is mainly dependent on cathode materials [3–5]. Therefore, extensive efforts have been devoted to exploring new cathode materials to further improve the electrochemical performance of LIBs.

Among the potential cathode materials, vanadium pentoxide (V_2O_5) has been extensively studied in recent years because of its low cost, abundance, ease of synthesis, as well as its high energy efficiency and relatively high theoretical capacity [6–8]. It is a typical intercalation compound with a layered crystal structure, which can act as a good host for the reversible insertion and extraction of Li^+. It can also attain a large theoretical capacity of 294 mAh g^{-1} in the voltage range of 4.0–2.0 V *vs.* Li/Li^+ [9,10]. This value is higher than those of commonly used cathode materials, such as $LiCoO_2$ (274 mAh g^{-1}), $LiMn_2O_4$ (148 mAh g^{-1}) and $LiFePO_4$ (170 mAh g^{-1}). However, the intrinsic low-diffusion coefficient of lithium ions ($D \sim 10^{-12}$ cm^2 s^{-1}) and poor electronic conductivity (10^{-2}–10^{-3} S cm^{-1}) in crystalline vanadium oxide (V_2O_5) hinder the practical application of this material [11–13].

To improve the diffusion capability of lithium ions in V_2O_5, development of nanostructured forms of V_2O_5 [9,13–17] has been demonstrated as an effective method due to the unique advantages offered by nanostructures over their bulk counterparts, including short Li^+ diffusion distance and large interfacial contact area between the electrode and electrolyte [18,19]. For example, nanostructured V_2O_5 prepared by thermal-decomposition of vanadyl oxalate could deliver an initial discharge capacity of 274 mAh g^{-1} at a low current density of C/20 (15 mA g^{-1}) while commercial micro-sized V_2O_5 only attained a capacity of ~100 mAh g^{-1} [13]. However, the electrochemical performance (including cyclability and rate capability) of the nanostructured V_2O_5 is still limited by its moderate electrical conductivity, vanadium dissolution, and aggregation of particles [20]. Thus, further performance improvement of the nanostructured V_2O_5-based cathode is required.

Currently, an effective approach to enhance the electrochemical performance is to hybridize nanostructured V_2O_5 with carbonaceous materials [21–24], since the hybridization of carbon can increase electrical conductivity, prevent the vanadium dissolution, and alleviate the aggregation of the particles. For instance, Dunn's group [21] incorporated V_2O_5 aerogels into single-walled carbon nanotubes and the composite material exhibited high capacities exceeding 400 mAh g^{-1}. As a new class of two-dimensional (2D) carbon nanostructure, graphene has been demonstrated as an excellent substrate to host active nanomaterials for energy

* Corresponding author. Tel.: +1 814 863 1287.
E-mail address: dwang@psu.edu (D. Wang).
[1] Current address: University, Hangzhou 310018, China.

0921-5107/$ – see front matter © 2014 Elsevier B.V. All rights reserved.
http://dx.doi.org/10.1016/j.mseb.2014.01.015

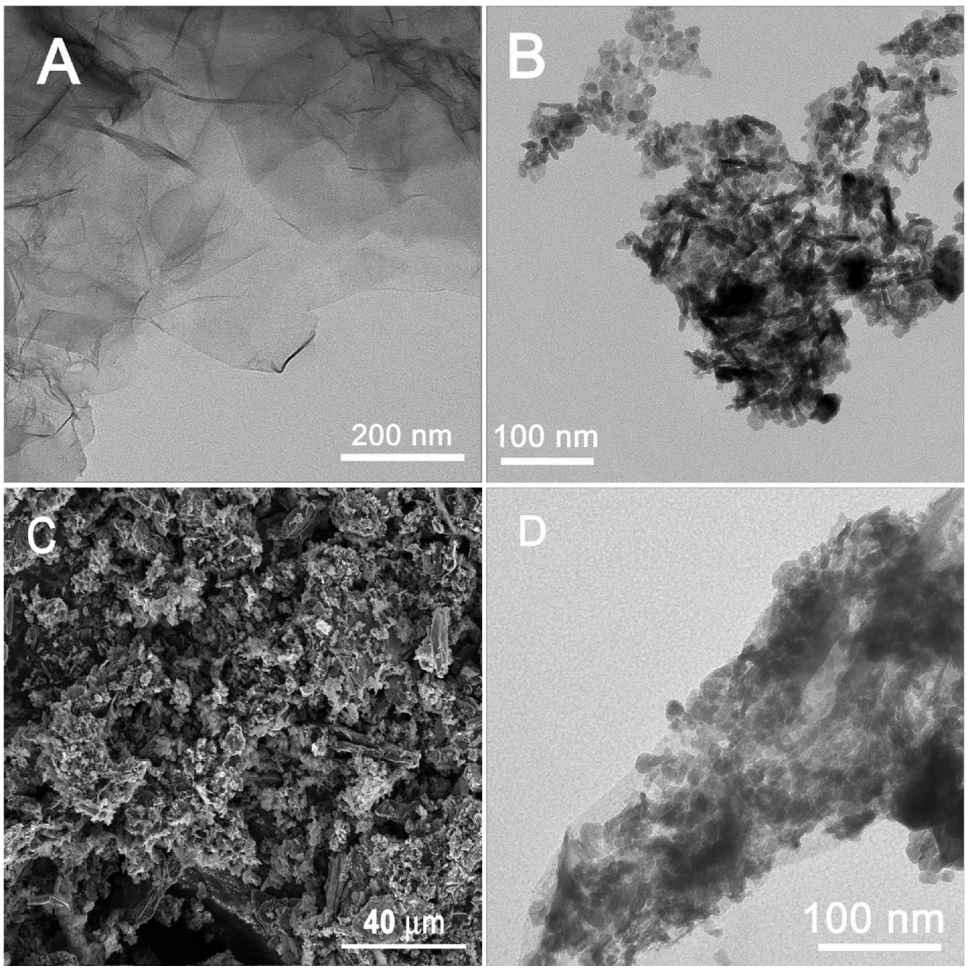

Fig. 1. Typical TEM images of the as-prepared (A) graphene oxide (GO) nanosheets, (B) V_2O_5 nanoparticles, (D) V_2O_5/graphene nanocomposites, and the SEM image (C) of V_2O_5/graphene nanocomposites.

applications due to its high conductivity, large surface area, flexibility, and chemical stability [25]. During the past few years, a number of studies have explored the fabrication of graphene-based composite electrode materials for LIBs, such as SnO_2/graphene [26], TiO_2/graphene [27], Co_3O_4/graphene [28], MoO_2/graphene [29], and Mn_3O_4/graphene [30]. All of these materials benefitted from the high electronic conductivity of 2D graphene and exhibited excellent electrochemical performance for lithium-ion storage. Inspired by these materials, recent studies have investigated the incorporation of graphene with V_2O_5 for the development of LIBs composite cathodes with superior performance; however, there are only a few reports on V_2O_5/graphene composite cathodes. These reports focused on 2D graphene nanosheets incorporated with different nanostructured V_2O_5, such as films [31], nanowires [32], porous spheres [33] and xerogels [34]. However, to the best of our knowledge, composites of graphene and V_2O_5 nanoparticles, have not been reported so far.

In this work, we report a facile solvothermal approach to synthesize the composite of V_2O_5 nanoparticles anchored on graphene as a cathode material for high performance LIBs. This V_2O_5/graphene nanocomposite displays superior LIB performance with large reversible capacity, high Coulombic efficiency, enhanced cyclic performance, and good rate capability, highlighting the importance of the anchoring of nanoparticles on graphene sheets for maximum utilization of electrochemically-active V_2O_5 nanoparticles in high-performance LIBs.

2. Experimental

Graphite oxide was prepared using a modified Hummers' method as described elsewhere [35], and vanadium (IV) acetylacetone was synthesized according to the literature [6]. The typical synthesis process of V_2O_5/graphene nanocomposites was described as follows. Firstly, the graphite oxide powders (40 mg) were dispersed in *N*,*N*-dimethyllformamide (DMF) by probe sonication for 30 min to form a stable graphene oxide (GO) dispersion (1 mg mL^{-1}). Then, vanadium (IV) acetylacetone (1 g) was dissolved into the prepared GO dispersion and stirred for about 1 h. A transparent solution was formed, which was transferred into a 50 mL Teflon-lined stainless steel autoclave. The autoclave was sealed and maintained at 200 °C for 20 h. After the solution was cooled down to room temperature, the obtained black precipitate was collected by centrifuging the mixture, which was then washed with absolute ethanol and distilled water several times and dried at 80 °C for 6 h. To obtain the V_2O_5/graphene nanocomposites, the as-prepared precipitate was subsequently pyrolyzed at 400 °C for 2 h under a heating rate of 10 °C min^{-1} in air. For comparison, V_2O_5 nanoparticles were also prepared by a similar procedure to that described above in the absence of GO.

Transmission electron microscope (TEM) measurements were conducted on a JEOL 1200 microscope at 200 keV. X-ray diffraction (XRD) patterns of the samples were measured on a Powder X-ray diffractometer (MiniFlex II, Rigaku) using Cu Kα radiation. Thermogravimetric analysis (TGA) and differential thermal analysis (DTA)

were carried out using a thermogravimetric analyzer (SDT 2960, TA instruments) with a heating rate of 5 °C min^{-1} in air.

Electrochemical properties of the products were measured using coin cells. The working electrodes were prepared by casting a slurry consisting of 80 wt% active material (*i.e.* as-prepared V_2O_5 nanoparticles or V_2O_5/graphene nanocomposites), 10 wt% conductive Super P carbon, and 10 wt% polyvinylidene fluoride (PVDF) onto aluminum foil. The electrolyte consisted of a solution of 1 M $LiPF_6$ in ethylene carbonate (EC)/diethyl carbonate (DEC) (1:1, v/v). Lithium foil served as counter electrodes. These cells were assembled in an argon-filled glovebox (Mbraun Labstar) and galvanostatically-cycled between 2.0 V and 4.0 V on a multi-channel battery cycler (Arbin Instruments). Cyclic voltammetry (CV) measurements were performed on an electrochemical workstation (CHI 660D) at a scan rate of 0.1 mV s^{-1} in the voltage range of 2–4 V. The AC impedance was measured using the same instrument in a frequency range of 10^5–0.001 Hz with a voltage amplitude of 5 mV.

3. Results and discussion

Fig. 1 shows the typical TEM images of as-prepared GO nanosheets, V_2O_5 nanoparticles, and V_2O_5/graphene nanocomposites as well as the SEM image of V_2O_5/graphene nanocomposites. The free-standing GO nanosheets (Fig. 1A) were not perfectly flat but displayed intrinsic microscopic roughening and out-of-plane deformations (wrinkles) with one or few layer sheet structure. The multilayered structure in GO may represent the parts that either have not been fully exfoliated or have restacked together due to capillary, electrostatic interaction and the van der Waals forces during the dispersion process [27,36]. The as-prepared V_2O_5 nanoparticles (Fig. 1B) were irregular with the average size of 20–40 nm and were prone to aggregation. As for the as-prepared V_2O_5/graphene nanocomposites, the overall morphologies were shown in Fig. 1C. It can be seen that graphene nanosheets were, on the whole, evenly combined with V_2O_5 nanoparticles, and the graphene sheets and V_2O_5 nanoparticles were distinguished clearly. The enlarged morphological image (Fig. 1D) further reveals that V_2O_5 nanoparticles were well distributed on the 2D graphene nanosheets, with the morphology and size of the distributed nanoparticles similar to the pure V_2O_5 nanoparticles.

Typical XRD patterns of the as-fabricated V_2O_5/graphene nanocomposites, together with the pure V_2O_5 nanoparticles, are displayed in Fig. 2. The XRD pattern of the V_2O_5 nanoparticles

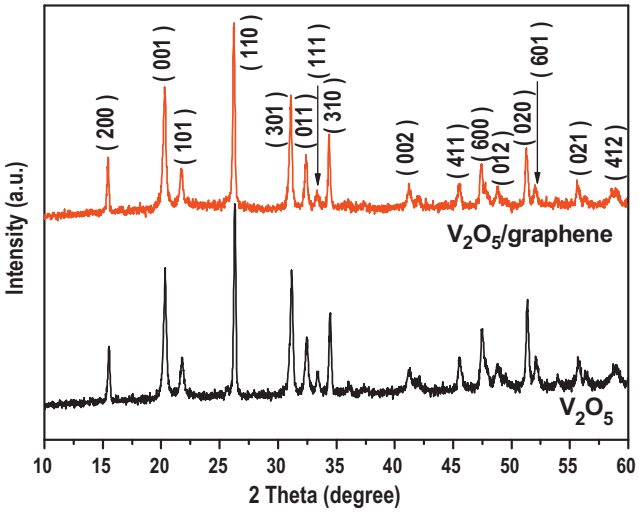

Fig. 2. XRD patterns for as-prepared V_2O_5 nanoparticles and V_2O_5/graphene nanocomposites after calcinations for 2 h at 400 °C in air.

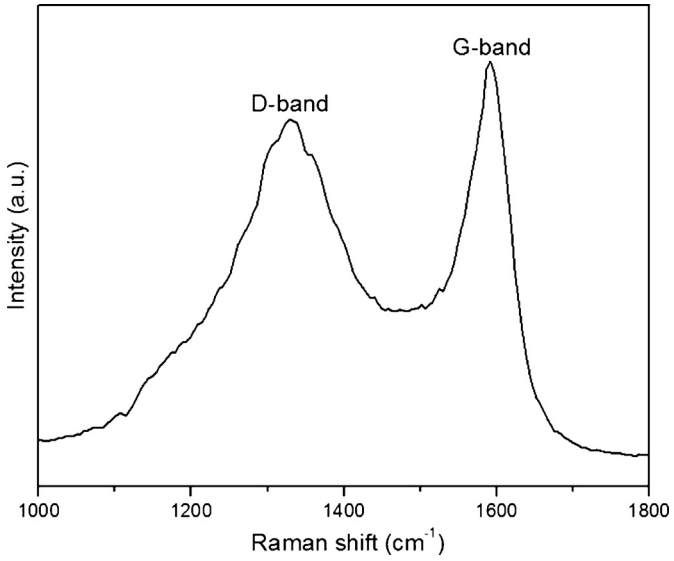

Fig. 3. Raman spectrum of the V_2O_5/graphene nanocomposites.

corresponded well to the orthorhombic structure with lattice parameters $a = 11.516$ Å, $b = 3.566$ Å, and $c = 4.373$ Å (JCPDS card no. 41-1426), and no other peaks were detected, indicating the high purity of as-synthesized V_2O_5 nanoparticles. According to the Scherrer method, crystallite dimensions of about 26 nm could be deduced from the (1 1 0) peak for the nanoparticles, which was in agreement with the above TEM results. In addition, V_2O_5/graphene nanocomposites showed a similar XRD pattern to pure V_2O_5, and no diffraction peaks of carbon species were observed in the composite, which might be due to the low mass content and relatively low diffraction intensity of graphene. Fig. 3 shows the Raman spectrum of the V_2O_5/graphene nanocomposite. Two peaks at 1333 and 1614 cm^{-1} can be observed, which correspond to the D (disordered) band and the G (graphite) band of carbon, respectively. These two peaks confirm the presence of graphene in the nanocomposite. To determine the weight percentage of graphene in the V_2O_5/graphene nanocomposites, TGA was carried out in air. As shown in Fig. 4, the weight loss of 1.14% below the temperature of 350 °C is attributed to the evaporation of moisture (including the physically absorbed or chemisorbed water molecules). The thermal decomposition of graphene mainly occurs at 400–600 °C, leading to a weight loss of 3.62%. Furthermore, evidence from the DTA curves

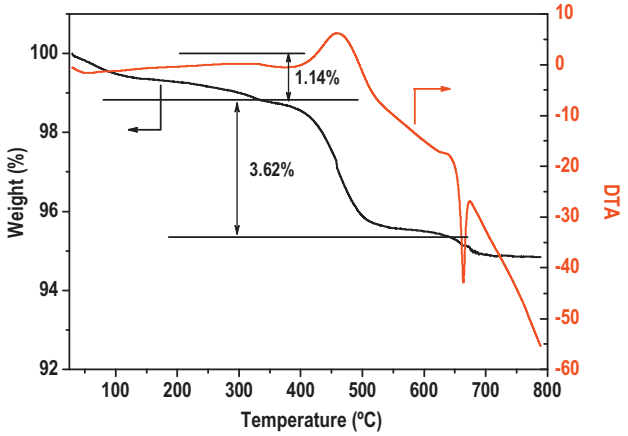

Fig. 4. TG-DTA curves of V_2O_5/graphene nanocomposites. The weight loss before 350 °C is ascribed to the physical absorbed or chemisorbed water molecular, and the weight loss before 600 °C is ascribed to the burning of graphene. At around 660 °C, the V_2O_5 is melted.

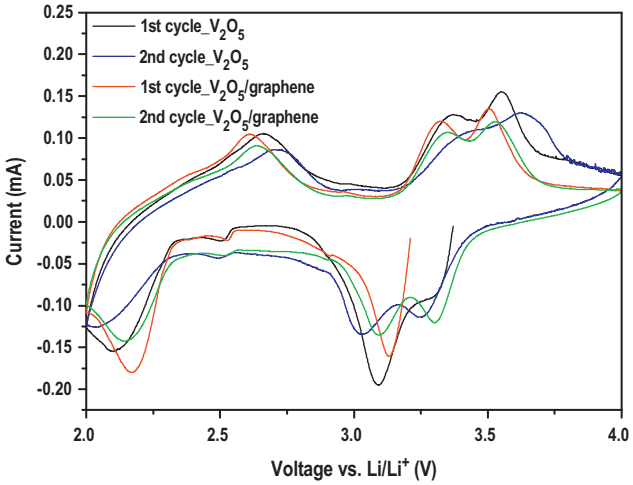

Fig. 5. The first two cycles of CV curves of the as-prepared V_2O_5, V_2O_5/graphene electrodes between 2 and 4 V at a scan rate of 0.1 mV s^{-1}.

also shows a large, relatively sharp exotherm peak at 400–500 °C due to the combustion of graphene in air. The remarkable endothermic peak located at 650 °C might represent the melting of vanadium oxide. Thus, excluding the weight of moisture, the final weight percentage of graphene was determined to be approximately 3.89 wt% in the composite.

Fig. 5 shows the first two cycles of CV curves of V_2O_5 and V_2O_5/graphene electrodes for lithiation–delithiation in the voltage range of 2–4 V *vs.* Li^+/Li. For the V_2O_5/graphene composite electrode, during a cathodic scan, three distinct peaks were shown at 3.31, 3.12 and 2.17 V *vs.* Li^+/Li, which indicated a multi-step lithiation process and the corresponding phase was transformed from α-V_2O_5 to ε-$Li_{0.5}V_2O_5$ (3.31 V), δ-LiV_2O_5 (3.12 V), and γ-$Li_2V_2O_5$ (2.17 V), consecutively [13,37]:

$$V_2O_5 + 0.5Li^+ + 0.5e^- \leftrightarrow Li_{0.5}V_2O_5 \quad (1)$$

$$Li_{0.5}V_2O_5 + 0.5Li^+ + 0.5e^- \leftrightarrow LiV_2O_5 \quad (2)$$

$$LiV_2O_5 + Li^+ + e^- \leftrightarrow Li_2V_2O_5 \quad (3)$$

In the following anodic scan, three peaks were observed at 2.61, 3.34, and 3.5 V *vs.* Li^+/Li. The first peak and the later two peaks were ascribed to the deintercalation of the second and first lithium ions [24]. Compared to the V_2O_5/graphene composite electrode, however, the V_2O_5 electrode also showed three pairs of redox peaks with three negatively shifted cathodic peaks and three positively shifted anodic peaks. It is clear that the difference between the cathodic and the anodic peaks for the V_2O_5/graphene composite electrode is much smaller than that for the bare V_2O_5 electrode under identical conditions. The potential difference between the cathodic and anodic peaks indicates the polarization of the cell. The cell polarization is induced by the cell resistance, which is related to the Li^+ ion transport into and through the electrode. This result clearly indicates that the kinetics of lithium deintercalation/intercalation in the V_2O_5/graphene nanocomposites was significantly improved by the quick migration of electrons between the V_2O_5 nanoparticles and graphene nanosheets. In addition, the voltage difference between the redox peaks of the bare V_2O_5 electrode for the second cycle is much larger than that for the first cycle, indicating the increase of polarization with cycling. Meanwhile, the peak intensity decreases with cycling. As for the V_2O_5/graphene composite electrode, similar results were obtained with a yet lower increase of the potential difference between anodic and cathodic peaks and a relatively lower decrease of the peak intensity with cycling. This reveals that the V_2O_5/graphene composite electrode possesses a better reversibility and higher cyclability than

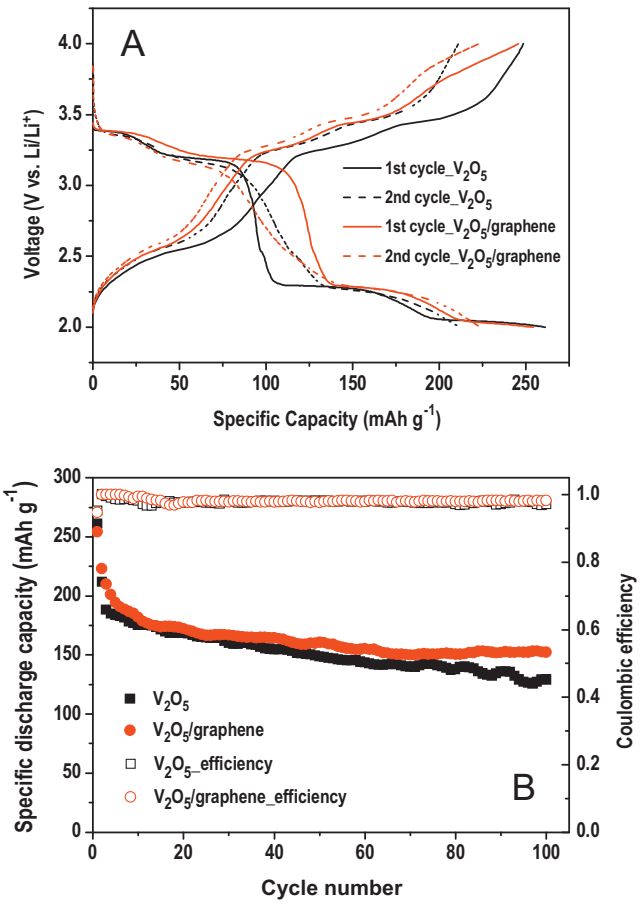

Fig. 6. (A) The first two cycles of charge/discharge curves of the as-prepared V_2O_5 and V_2O_5/graphene electrodes between 2 and 4 V at a current density of 100 mA g^{-1}. (B) Capacity (left) and efficiency (right) *versus* cycle number for the as-prepaedV_2O_5 and V_2O_5/graphene electrodes between 2 and 4 V at a current density of 100 mA g^{-1}.

the bare V_2O_5 electrode. Furthermore, two extra weak cathodic peaks at ~2.43 and ~2.8 V for both samples (V_2O_5 nanoparticles and graphene/V_2O_5 nanocomposites) were observed, and might be assigned to the phase transition of the impurity of $V_2O_5 \cdot xH_2O$ [10,34].

The Li^+ insertion/extraction properties of V_2O_5/graphene nanocomposites as a cathode material were investigated by galvanostatic charge-discharge measurements. Fig. 6A shows the first two charge/discharge curves of the V_2O_5 and V_2O_5/graphene electrodes in the voltage window of 2.0–4.0 V *vs.* Li^+/Li at a current density of 100 mA g^{-1}. According to the figure, three typical plateaus, in agreement with the above CV test results, were observed in both samples, which corresponded to a series of phase transitions of crystalline V_2O_5 during the lithiation–delithiation process. In the case of the bare V_2O_5 electrode, the first specific discharge capacity was 261 mAh g^{-1} with an initial Coulombic efficiency of 95%, while the discharge capacity for the second cycle dropped to 211 mAh g^{-1} (~80.8% of the initial discharge capacity) with a Coulombic efficiency of 99.6%. In contrast, the V_2O_5/graphene composite electrode displayed an initial specific discharge capacity of 255 mAh g^{-1} with the initial Coulombic efficiency of 96.5%. Compared with the bare V_2O_5 electrode, the V_2O_5/graphene composite electrode showed improved capacity retention of 224 mAh g^{-1} (~87.8% of the initial discharge capacity) for the second cycle with an efficiency of 99.8%. In addition, the V_2O_5/graphene composite electrode also exhibited improved cyclability. Fig. 6B shows the cycle performance of the bare V_2O_5 and V_2O_5/graphene electrodes between 2 and 4 V at a current

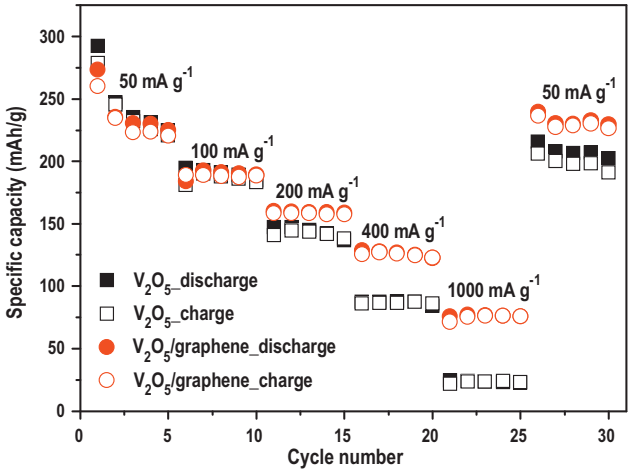

Fig. 7. Capacity performances at various cycling rates for as-prepared V_2O_5 nanoparticles and V_2O_5/graphene nanocomposites.

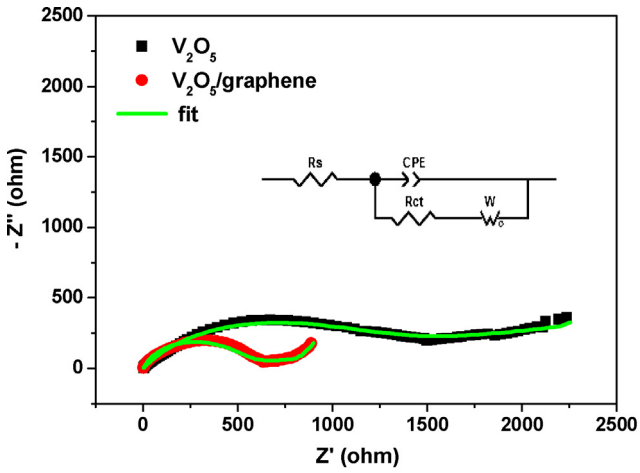

Fig. 8. Nyquist plots of as-prepared V_2O_5, V_2O_5/graphene electrodes using voltage amplitude of 5 mV from 100 kHz to 1 mHz. The high-middle frequency semicircle represents the charge-transfer process and a straight slopping line at low frequencies corresponds to the Warburg impedance. The inset is the equivalent circuit used to fit the impedance data.

density of 100 mA g^{-1} for the first 100 cycles. For the bare V_2O_5 electrode, a discharge capacity of 129 mAh g^{-1} was delivered at the 100th cycle, corresponding to 49.4% of the initial capacity, and the capacity fading rate was then estimated to be 0.506% per cycle. However, the V_2O_5/graphene composite electrode displayed a discharge capacity of 153 mAh g^{-1} after 100 cycles, which was 60.3% of the initial discharge capacity. The capacity fading rate was then calculated to be 0.397% per cycle, indicating that the introduction of graphene improves the cycling stability of the V_2O_5 nanoparticles. Moreover, it should be noted that, for the V_2O_5/graphene composite electrode, the major decay existed in the first 20 cycles with a fading rate of 4.2 mAh g^{-1} per cycle, which was almost four times that of the latter 80 cycles. The large irreversible capacity loss in the initial 20 cycles should be associated with the following irreversible phenomena: the inevitable formation of a solid electrolyte interface (SEI) film, the electrolyte decomposition and the structural change during the lithiation and delithiation process [38].

Fig. 7 shows the rate capability of the bare V_2O_5 and V_2O_5/graphene composite electrodes. The latter delivered reversible capacities of about 160, 129, and 76 mAh g^{-1} at a high discharge rate of 200, 400, and 1000 mA g^{-1}, respectively, whereas the bare V_2O_5 electrode examined under the same conditions only displayed 147, 87, and 24 mAh g^{-1}, respectively. To further understand the improved high-rate performance, the AC impedance characterization for the as-prepared V_2O_5 and V_2O_5/graphene composite electrodes was performed using electrochemical impedance spectroscopy (EIS) after rate capability testing at delithiated state. Fig. 8 shows the Nyquist plots of the as-prepared V_2O_5 and V_2O_5/graphene composite electrodes. Both spectra consist of a depressed semicircle in the high-to-medium frequency range and a straight line in the low frequency range. An equivalent circuit (inset in Fig. 8) is built to analyze the impedance spectra of the both samples. In this circuit, R_s presents the solution resistance, R_{ct} stands for the charge transfer resistance, *CPE* is the double layer capacitance, and *W* is the Warburg impedance. The electrochemical parameters of the two samples are simulated by *Z*-view software, and a good agreement between experimental and fitted data obtained from the equivalent circuit can be seen from Fig. 8. It is clearly shown that the V_2O_5/graphene composite electrode exhibited a much smaller charge-transfer resistance (0.63 kΩ) than the bare V_2O_5 electrode (1.45 kΩ), indicating the enhanced ionic conductivity and faster charge transfer of the V_2O_5/graphene composite electrode. This enhancement could be ascribed to the high conductivity of graphene, as well as the high surface area and porous structure of the graphene, which can facilitate the penetration of the electrolyte. Overall, the increased electrical conductivity and the favorable electrolyte penetration of the V_2O_5/graphene composite can significantly improve kinetics of the electrochemical processes, the fast Li^+ transport, and the structural stability during the lithiation/delithiation process, which could explain the increase in the cycling and rate performance of the V_2O_5/graphene composite.

From the electrochemical results above, it is clear that the anchoring of V_2O_5 nanoparticles with graphene plays an important role in improving the electrochemical performance. The high reversible capacity, improved cycle stability, and rate performance could be attributed to the following reasons. First, the highly conductive graphene nanosheets can improve the surface electrical conductivity of V_2O_5, providing electron percolation paths from the current collector to the surface area of individual V_2O_5 nanoparticles. Second, the porous structure of the graphene sheets is favorable for penetration of the electrolyte into the electrode, and the nanosized V_2O_5 creates short diffusion paths for lithium ions. Third, the well-crystallized V_2O_5 nanoparticles ensure the reversible phase transition. In addition, it can be deduced that the uniform mixture and interaction of V_2O_5 nanoparticles and graphene nanosheets prevent the aggregation of V_2O_5 nanoparticles, which likely maintains the electrode structures during the cycling process.

4. Conclusions

In summary, V_2O_5/graphene nanocomposites composed of V_2O_5 nanoparticles anchored to graphene nanosheets were successfully prepared by using a simple solvothermal approach. Compared with the bare V_2O_5 nanoparticles, the V_2O_5/graphene nanocomposites exhibited a significant improvement in electrochemical performance of the LIBs, shown by highly reversible capacities, good cycling stabilities, and excellent rate capabilities. This enhancement was ascribed to the unique structure of the composite, which could increase the electronic and ionic conductivity of the electrodes by forming an efficient conductive network and maintain the structural integrity of the composite electrodes by helping accommodate large volume changes and prevent particle agglomeration. This work on graphene nanosheets as the carbon matrix in a composite material could be extended to other metal oxides.

Acknowledgements

This work was supported by the Assistant Secretary for Energy Efficiency and Renewable Energy, Office of Vehicle Technologies of the U.S. Department of Energy under Contract No. DE-AC02-05CH11231, Subcontract No. 6951378 under the Batteries for Advanced Transportation Technologies (BATT) Program.

References

[1] R. Yi, F. Dai, M.L. Gordin, S.R. Chen, D.H. Wang, Adv. Energy Mater. 3 (2013) 295.
[2] B.B. Owens, W.H. Smyrl, J.J.L. Xu, J. Power Sources 81–82 (1999) 150.
[3] Y.G. Guo, Y.S. Hu, J. Maier, Chem. Commun. 26 (2006) 2783.
[4] Y.F. Shi, B.K. Guo, S.A. Corr, Q.H. Shi, Y.S. Hu, K.R. Heier, L.Q. Chen, R. Seshadri, G.D. Stucky, Nano Lett. 9 (2009) 4215.
[5] J.W. Fergus, J. Power Sources 195 (2010) 939.
[6] J. Liu, H. Xia, D.F. Xue, L. Lu, J. Am. Chem. Soc. 131 (2009) 12086.
[7] D.M. Yu, S.T. Zhang, D.W. Liu, X.Y. Zhou, S.H. Xie, Q.F. Zhang, Y.Y. Liu, G.Z. Cao, J. Mater. Chem. 20 (2010) 10841.
[8] S.Q. Wang, S.R. Li, Y. Sun, X.Y. Feng, C.H. Chen, Energy Environ. Sci. 4 (2011) 2854.
[9] C.K. Chan, H. Peng, R.D. Twesten, K. Jarausch, X.F. Zhang, Y. Cui, Nano Lett. 7 (2007) 490.
[10] X.H. Rui, J.X. Zhu, W.L. Liu, H.T. Tan, D.H. Sim, C. Xu, H. Zhang, J. Ma, H.H. Hng, T.M. Lim, Q.Y. Yan, RSC Adv. 1 (2011) 117.
[11] J. Muster, G.T. Kim, V. Krstic, J.G. Park, Y.W. Park, S. Roth, M. Burghard, Adv. Mater. 12 (2000) 420.
[12] T. Watanabe, Y. Ikeda, T. Ono, M. Hibino, M. Hosoda, K. Sakai, T. Kudo, Solid State Ionics 151 (2002) 313.
[13] A.Q. Pan, J.G. Zhang, Z.M. Nie, G.Z. Cao, B.W. Arey, G.S. Li, S.Q. Liang, J. Liu, J. Mater. Chem. 20 (2010) 9193.
[14] A.M. Cao, J.S. Hu, H.P. Liang, L.J. Wan, Angew. Chem. Int. Ed. 44 (2005) 4391.
[15] P. Liu, S.H. Lee, C.E. Tracy, Y. Yan, J.A. Turner, Adv. Mater. 14 (2007) 27.
[16] E.A. Olivetti, K.C. Avery, I. Taniguchi, D.R. Sadoway, A.M. Mayes, J. Electrochem. Soc. 155 (2008) A488.
[17] Y.S. Hu, X. Liu, J.O. Müller, R. Schlögl, J. Maier, D.S. Su, Angew. Chem. Int. Ed. 48 (2009) 210.
[18] A. Singhal, G. Skandan, G. Amatucci, F. Badway, N. Ye, A. Manthiram, H. Ye, J.J. Xu, J. Power Sources 129 (2004) 38.
[19] Y. Wang, K. Takahashi, K. Lee, G. Cao, Adv. Funct. Mater. 16 (2006) 1133.
[20] K. West, B. Zachau-Christiansen, T. Jacobsen, S. Skaarup, Electrochim. Acta 38 (1993) 1215.
[21] J.S. Sakamoto, B. Dunn, J. Electrochem. Soc. 149 (2002) A26.
[22] S. Suzuki, M. Hibino, M. Miyayama, J. Power Sources 124 (2003) 513.
[23] H. Yamada, K. Tagawa, M. Komatsu, I. Moriguchi, T. Kudo, J. Phys. Chem. C 111 (2007) 8397.
[24] M. Koltypin, W. Pol, A. Gedanken, D. Aurbach, J. Electrochem. Soc. 154 (2007) A605.
[25] D. Chen, L.H. Tang, J.H. Li, Chem. Soc. Rev. 39 (2010) 3157.
[26] S.M. Paek, E. Yoo, I. Honma, Nano Lett. 9 (2009) 72.
[27] D.H. Wang, D.W. Choi, J. Li, Z.G. Yang, Z.M. Nie, R. Kou, D.H. Hu, C.M. Wang, L.V. Saraf, J.G. Zhang, I.A. Aksay, J. Liu, ACS Nano 3 (2009) 907.
[28] S.B. Yang, X.L. Feng, S. Ivanovici, K. Mullen, Angew. Chem. Int. Ed. 49 (2010) 8408.
[29] Y. Xu, R. Yi, B. Yuan, M. Dunwell, Q.L. Lin, L. Fei, S.G. Deng, P. Andersen, D.H. Wang, H.M. Luo, J. Phys. Chem. Lett. 3 (2012) 309.
[30] H.L. Wang, L.F. Cui, Y. Yang, H.S. Casalongue, J.T. Robinson, Y. Liang, Y. Cui, H.J. Dai, J. Am. Chem. Soc. 132 (2010) 13978.
[31] H. Gwon, H.S. Kim, K.U. Lee, D.H. Seo, Y.C. Park, Y.S. Lee, B.T. Ahn, K. Kang, Energy Environ. Sci. 4 (2011) 1277.
[32] H.M. Liu, W.S. Yang, Energy Environ. Sci. 4 (2011) 4000.
[33] X.H. Rui, J.X. Zhu, D.H. Sim, C. Xu, Y. Zeng, H.H. Hng, T.M. Lim, Q.Y. Yan, Nanoscale 3 (2011) 4752.
[34] G.D. Du, K.H. Seng, Z.P. Guo, J. Liu, W.X. Li, D.Z. Jia, C. Cook, Z.W. Liu, H.K. Liu, RSC Adv. 1 (2011) 690.
[35] Y.X. Xu, H. Bai, G.W. Lu, C. Li, G.Q. Shi, J. Am. Chem. Soc. 130 (2008) 5856.
[36] M.J. McAllister, J.L. Li, D.H. Adamson, H.C. Schniepp, A.A. Abdala, J. Liu, M. Herrera-Alonso, D.L. Milius, R. Car, R.K. Prud'homme, I.A. Aksay, Chem. Mater. 19 (2007) 4396.
[37] S.H. Ng, T.J. Patey, R. Büchel, F. Krumeich, J.Z. Wang, H.K. Liu, S.E. Pratsinis, P. Novák, Phys. Chem. Chem. Phys. 11 (2009) 3748.
[38] S.Q. Wang, Z.D. Lu, D. Wang, C.G. Li, C.H. Chen, Y.D. Yin, J. Mater. Chem. 21 (2011) 6365.